Counter-Rotating Streamwise Vortex Formation in the Turbine Cascade with Endwall Fence

고성룡[1], 문영준[2]
Seong Ryong Koh and Young J. Moon

The three-dimensional turbulent cascade flows with and without endwall fences are numerically investigated by solving the incompressible Navier-Stokes equations with a high-Reynolds number $k-\varepsilon$ turbulence closure model. A projection method based algorithm is used in the finite-volume formulation, with the second order upwind-differencing scheme for the convective terms. First, assessments on accuracy of the present method are made by comparing the static pressure distributions at the mid-span of the cascade with measured data, and also by confirming the experimental observations on the choice of an optimal fence height for the secondary flow control. In understanding the three-dimensional nature of the secondary flow in turbine cascade, the limiting streamline patterns and the static pressure contours at the suction surface of the blade as well as on the cascade endwall are employed to visualize the effectiveness of the endwall fence for the secondary flow control. Analysis on the streamwise vorticity contour maps along the cascade with the three-dimensional representation of their iso-surfaces reveals the strucuture of the complicated vortical flow in the turbine cascade with endwall fence, and also leads to an understanding on formation of the counter-rotating streamwise vortex over the endwall fence, in explaining the mechanisms of controlling the secondary flow and also for the proper selection of an optimal fence height.

1. INTRODUCTION

In the three-dimensional turbine cascade, a secondary flow is generated by the interaction of the horseshoe vortex generated upstream from the blade leading edge with the passage vortex due to the curvature effect of the bend. The pressure-side leg of the horseshoe vortex rotates in the same direction as the passage vortex, and as a result these two are superposed as shown schematically in Fig. 1. In control of the secondary flow, Kawai[1-4] and Chung[5] have experimentally investigated on use of the boundary layer fence at the endwall region to hinder the mergence of the horseshoe vortex with the passage vortex, and have measured the total pressure losses and velocity distributions at the wake region. An optimal size and location of the boundary layer fence was determined by observing the fact that a fence with 1/3 height of the inlet boundary layer thickness located in the middle between blades reduces the secondary flow loss by 20 percents.

In the present work, the incompressible Navier-Stokes equations are numerically solved with a high Reynolds number $k-\varepsilon$ turbulence closure model for the analysis of the three-dimensional turbulent cascade flows with and without fences. Our concerns lie on accurate numerical prediction of the secondary flow in cascade as well as on understanding of its three-dimensional flow structures. Objectives of the present study are to investigate how the boundary layer fence reduces the secondary flow development in the cascade, and to understand why the fence with 1/3 height of the inlet boundary layer thickness is optimal for the secondary flow control.

2. MATHEMATICAL FORMULATION

A turbulence closure is made by solving the standard $k-\varepsilon$ equations. A non-dimensional form of the $k-\varepsilon$ turbulence transport equations in generalized coordinates is written as

1) 고려대학교 기계공학과 대학원
2) 고려대학교 기계공학과 (136-701, 서울특별시 성북구 안암5가 1)

$$\frac{\partial \widehat{Q}_t}{\partial t}+\frac{\partial \widehat{E}_t}{\partial \xi}+\frac{\partial \widehat{F}_t}{\partial \eta}+\frac{\partial \widehat{G}_t}{\partial \zeta}=\frac{\partial \widehat{E_{vt}}}{\partial \xi}+\frac{\partial \widehat{F_{vt}}}{\partial \eta}+\frac{\partial \widehat{G_{vt}}}{\partial \zeta}+\widehat{S}_t \tag{1}$$

where, the turbulence dependent variable vector, and the convective and viscous flux vectors are defined as follows:

$$\widehat{Q}_t=\frac{1}{J}\begin{bmatrix} k \\ \varepsilon \end{bmatrix},\quad \widehat{E}_t=\frac{1}{J}\begin{bmatrix} kU \\ \varepsilon U \end{bmatrix},\quad \widehat{F}_t=\frac{1}{J}\begin{bmatrix} kV \\ \varepsilon V \end{bmatrix},\quad \widehat{G}_t=\frac{1}{J}\begin{bmatrix} kW \\ \varepsilon W \end{bmatrix} \tag{2}$$

and

$$\widehat{E_{vt}}=\frac{1}{ReJ}\begin{bmatrix} \left(\frac{\nu_t}{\sigma_k}\right)\left\{\nabla\xi\cdot\nabla\xi\frac{\partial k}{\partial\xi}+\nabla\xi\cdot\nabla\eta\frac{\partial k}{\partial\eta}+\nabla\xi\cdot\nabla\zeta\frac{\partial k}{\partial\zeta}\right\} \\ \left(\frac{\nu_t}{\sigma_\varepsilon}\right)\left\{\nabla\xi\cdot\nabla\xi\frac{\partial \varepsilon}{\partial\xi}+\nabla\xi\cdot\nabla\eta\frac{\partial \varepsilon}{\partial\eta}+\nabla\xi\cdot\nabla\zeta\frac{\partial \varepsilon}{\partial\zeta}\right\} \end{bmatrix}$$

$$\widehat{F_{vt}}=\frac{1}{ReJ}\begin{bmatrix} \left(\frac{\nu_t}{\sigma_k}\right)\left\{\nabla\eta\cdot\nabla\xi\frac{\partial k}{\partial\xi}+\nabla\eta\cdot\nabla\eta\frac{\partial k}{\partial\eta}+\nabla\eta\cdot\nabla\zeta\frac{\partial k}{\partial\zeta}\right\} \\ \left(\frac{\nu_t}{\sigma_\varepsilon}\right)\left\{\nabla\eta\cdot\nabla\xi\frac{\partial \varepsilon}{\partial\xi}+\nabla\eta\cdot\nabla\eta\frac{\partial \varepsilon}{\partial\eta}+\nabla\eta\cdot\nabla\zeta\frac{\partial \varepsilon}{\partial\zeta}\right\} \end{bmatrix}$$

$$\widehat{G_{vt}}=\frac{1}{ReJ}\begin{bmatrix} \left(\frac{\nu_t}{\sigma_k}\right)\left\{\nabla\zeta\cdot\nabla\xi\frac{\partial k}{\partial\xi}+\nabla\zeta\cdot\nabla\eta\frac{\partial k}{\partial\eta}+\nabla\zeta\cdot\nabla\zeta\frac{\partial k}{\partial\zeta}\right\} \\ \left(\frac{\nu_t}{\sigma_\varepsilon}\right)\left\{\nabla\zeta\cdot\nabla\xi\frac{\partial \varepsilon}{\partial\xi}+\nabla\zeta\cdot\nabla\eta\frac{\partial \varepsilon}{\partial\eta}+\nabla\zeta\cdot\nabla\zeta\frac{\partial \varepsilon}{\partial\zeta}\right\} \end{bmatrix} \tag{3}$$

The source vector is given by

$$\widehat{S}_t=\frac{1}{J}\begin{bmatrix} G-\varepsilon \\ \frac{C_1\varepsilon}{k}G-\frac{C_2\varepsilon^2}{k} \end{bmatrix} \tag{4}$$

where the generation term G is defined as

$$G=\nu_t\left(\frac{\partial u_i}{\partial\xi_l}\frac{\partial\xi_l}{\partial x_j}+\frac{\partial u_j}{\partial\xi_l}\frac{\partial\xi_l}{\partial x_i}\right)\frac{\partial u_i}{\partial\xi_l}\frac{\partial\xi_l}{\partial x_j} \tag{5}$$

and the standard constants of $C_\mu=0.09$, $C_1=1.44$, $C_2=1.92$, $\sigma_k=1$, $\sigma_\varepsilon=1.217$ are used in practice, and a wall function is employed for the wall treatment.

In the present study, the velocity and pressure fields are solved in a coupled manner by a projection method based procedure. The governing equations are discretized by following a cell-center based finite-volume formulation, and the second order upwind differencing scheme is applied to the convective flux terms. Here, the transported variables at the cell face are determined by a linear extrapolation from each upwind direction, while the contravariant material velocity and the pressure at the cell face are defined by a linear interpolation between two neighboring cells. This differencing procedure may result in an odd-even decoupling of the pressure field, and therefore a momentum linear interpolation technique proposed by Rhie and Chow [6] is used. For the steady flow calculation, convergence acceleration methods such as local time stepping and implicit residual smoothing are used in conjunction with the basic time integrator. In the present method, the Poisson equation is implicitly solved by an alternate directional implicit (ADI) method with a single sweep, and a Neumann type boundary condition is used. The turbulence transport equations (1)-(5) are also solved by following the same numerical procedures described in this section.

3. RESULTS AND DISCUSSION

3.1. Secondary flow in turbine cascade

A turbine cascade in the experiment of Wang et al. [7] is considered in the present numerical study, except that the aspect ratio is modified to 2.0. The blade profile and its coordinate system are illustrated in Fig. 2, where x and y indicate the axial and pitch directions and z the spanwise direction. A three-dimensional turbulent cascade flow is computed for $Re_{ex}=5.4\times10^5$ and turbulent intensity 0.7 %. Here the subscription ex denotes a basis for an exit velocity. Figure 3 shows the computational grid of the blade passage in a perspective view and the mesh details near the leading and trailing edges of the blade. The blade definition is given in Ref. [7], and its geometrical details are summarized in Table 1. Accuracy assessment of the present numerical method as well as the grid independency test are conducted. The static pressure distributions at the mid-span of the cascade are compared in Fig. 4 with measured data [7] among various computational grids. The results obtained by using a two-dimensional approximation are also closely compared with measurement, but not quite accurately matched as the three-dimensional results. This discrepancy protrudes at the suction surface of the cascade near the trailing edge due to the effect of the secondary flow development. The three-dimensional grid of $95\times40\times40$ points in axial, pitch, and spanwise directions yields the closest solution to the experiment. An iso-surface of the non-dimensional streamwise vorticity $(C\omega_s/U=5)$ well represents the three- dimensional nature of the turbine cascade flow (see Fig. 5). The figure clearly shows the secondary flow structure within the cascade, i.e. the mergence of the stretched pressure-side leg of the horseshoe vortex generated upstream of the blade leading edge with the passage vortex developed within a curved cascade profile. The flow patterns and size of the secondary flow are distinctively identifiable in Fig. 7 by the limiting streamlines on the cascade endwall and suction surface of the blade.

3.2. Counter-rotating streamwise vortex formation with endwall fence

A fence of 5 mm thickness is mounted on the cascade endwall to suppress the secondary flow development by hindering the interaction of an upcoming horseshoe vortex from the turbine leading edge with the passage vortex. The fence profile is same as the blade camberline, and three fences of 1/3, 2/3, and 3/3 heights of the inlet boundary layer thickness are tested as in the experiments [1-5]. Also the same flow conditions are used as in the previous case. Figure 6 shows the endwall fence of the highest case $(h_f=3\delta/3)$ modeled on a computational grid. Here h_f denotes the fence height and δ the inlet boundary layer thickness. The static pressure coefficient contours and limiting streamlines presented in Fig. 7 reveal the structures of the three-dimensional cascade flows with and without endwall fences. From Fig. 7(a) & (b), one can clearly recognize the size of the secondary flow developed within the cascade for each case. With endwall fence, the secondary flow development near the suction surface is much suppressed, and an optimal fence height for the secondary flow control is clearly discernable from the figures. From the limiting streamline patterns on the endwalls as shown in Fig. 7(c), one can see the flow topology near the endwall surface and understand how the flow structure is altered by inserting a fence. A saddle point is clearly visible near the blade leading edge due to the horseshoe vortex formation, and the right-hand leg of the horseshoe vortex leaning to the suction side is blocked by the fence. It can also be noticed that a strong cross-flow from the pressure to suction side on the cascade endwall is considerably reduced by the boundary layer fences, and that, as the fence height increases, the development of the cross-flow becomes stronger in the region between fence and the suction surface. With the fence of 1/3 height of the inlet boundary layer thickness, the secondary flow is least developed, which, in fact, agrees well with the experimental observations made by Kawai [1-4] and Chung [5]. One can also observe that, as the fence height increases, the blocking point of the divided streamline moves downstream due to the blockage effect. It is known that the

secondary flow development is mainly due to the mergence of the horseshoe vortex with the passage vortex. Therefore it may be simply conjectured that a complete blocking of the horseshoe vortex will reduce the secondary flow development, since the mergence of these two counter-clockwise rotating vortexes is prohibited. On the contrary, the secondary flow near the suction surface becomes stronger, as the fence height increases.

The interaction mechanisms of the horseshoe vortex with the boundary layer fence and the formation of a counter-rotating streamwise vortex in the cascade are three-dimensionally visualized in Fig. 8 by the iso-surfaces of the non-dimensional streamwise vorticity of +15 (counter-clockwise rotating horseshoe and passage vortexes in dark color) and -15 (clockwise rotating streamwise vortex in light color). The large scale structure of the merged passage vortex rotating in a positive direction in the cascade with no endwall fence is clearly shown in Fig. 8(a), whereas, for the case of $h_f = 1\delta/3$ in Fig. 8(b), one can see the right-hand leg of the horseshoe vortex continuously scraping the fence edge from upstream and generating a counter-rotating streamwise vortex in the region between the fence and the suction surface. Figure 8(d) shows that, for the case with the highest fence, the horseshoe vortex is almost completely blocked by the fence and there is no formation of a counter-rotating streamwise vortex in the cascade. The effectiveness of reducing the passage vortex near the suction surface (shown as a dark iso-surface of the positive streamwise vorticity) is clearly noticeable among cases from Fig.'s 8(a)-(d).

4. CONCLUDING REMARKS

It is lead to a conclusion that understanding on formation of the counter-rotating streamwise vortex in the turbine cascade with endwall fence explains the mechanisms of controlling the secondary flow development and also for the proper selection of an optimal fence height.

REFERENCES

[1] Kawai, T., Adachi, T. and Shinoki, S., "Secondary Flow Control and Loss Reduction in a Turbine Cascade Using Endwall Fences". JSME Int. J. Ser. II, 32(3), 375-387, 1989.

[2] Kawai, T., Adachi, T. and Shinoki, S., "Visualization Study of Three-Dimensional Flows in a Turbine Cascade Endwall Region". JSME Int. J. Ser. II, 33(2), 256-264, 1989.

[3] Kawai, T., Adachi, T. and Shinoki, S., "Improvement in Turbine Blade Aerodynamic Force in the Tip Region". JSME Int. J. Ser. II, 33(3), 517-524, 1990.

[4] Kawai, T., "Effect of Combined Boundary Layer Fences on Turbine Secondary Flow and Losses". JSME Int. J. Ser. B, 37(2), 377-384, 1994.

[5] Chung, J.T., Simon, T.W. and Buddhavarapu, T., "Three-Dimensional Flow near the Blade/Endwall Junction of a Gas Turbine: Application of a Boundary Layer Fence". ASME Paper 91-GT-45, 1991.

[6] Rhie, C.M. and Chow, W.L., "Numerical Study of the Turbulent Flow past an Airfoil with Trailing Edge Separation". AIAA J., 21(11), 1525-1532, 1983.

[7] Wang, H., Olson, S.J., Goldstein, R.J. and Eckert, E.R.G., "Flow Visualization in a Linear Turbine Cascade of High Performance Turbine Blades". ASME Paper 95-GT-7, 1995.

Table 1. Turbine cascade geometry.

Chord Length (C)	184.15mm
Axial Chord to Chord Ratio (C_{ax}/C)	0.704
Aspect Ratio (H/C)	2.0
Solidity (C/P)	0.75
Blade Inlet Angle (β_1)	-35^o
Blade Outlet Angle (β_2)	72.5^o
Turning Angle	107.5^o
Incidence Angle	0^o

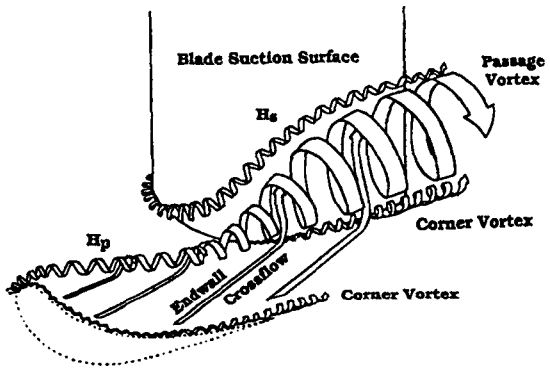

Fig. 1 Vortex system in the turbine cascade.

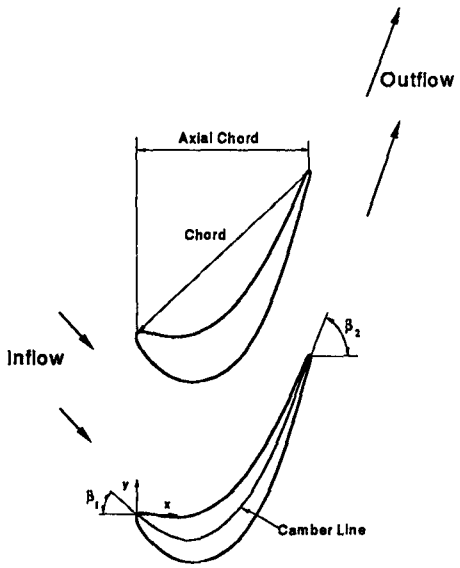

Fig. 2 Turbine blade definitions and coordinate system.

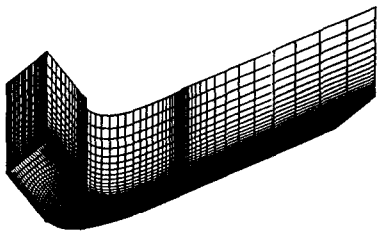

(a) Surface grids of a blade passage.

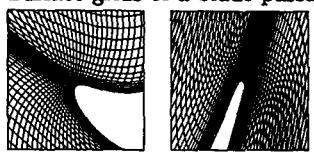

(b) Mesh details near the leading and trailing edges.

Fig. 3 Computational grid of a turbine cascade.

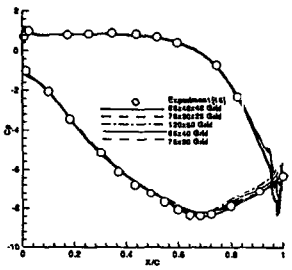

Fig. 4 Static pressure coefficient comparison among various grid sizes.

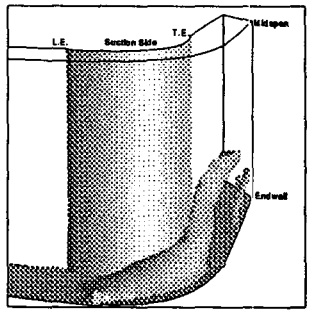

Fig. 5 An iso-surface of the non-dimensional streamwise vorticity ($C\omega_s/U = 5$), visualizing the structure of the secondary flow.

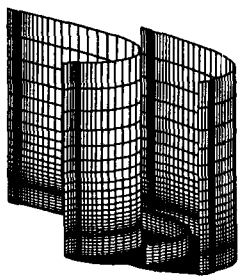

Fig. 6 An endwall fence ($h_f = \frac{3}{5}\delta$) modeled on a computational grid.

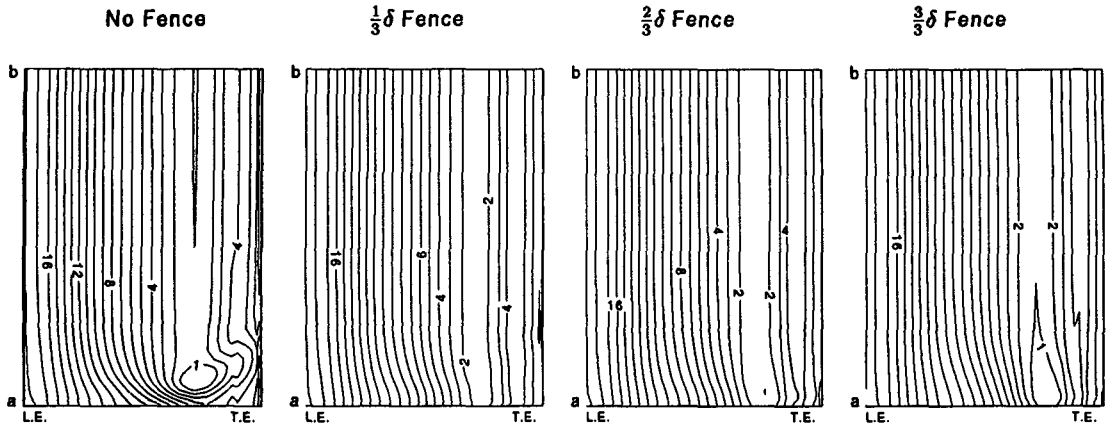

Level	1	2	4	6	8	10	12	14	16
Cp	-9.5	-9.0	-8.0	-7.0	-6.0	-5.0	-4.0	-3.0	-2.0

(a) Contour plots of static pressure coefficient at the suction surface.
(a:endwall, b:mid-span)

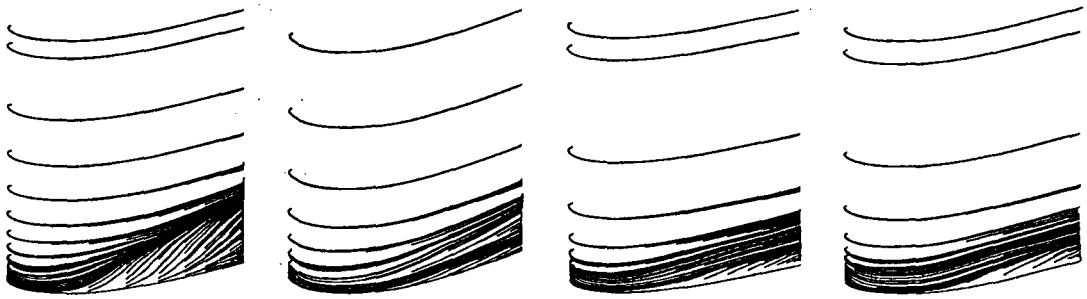

(b) Limiting streamlines at the suction surface.

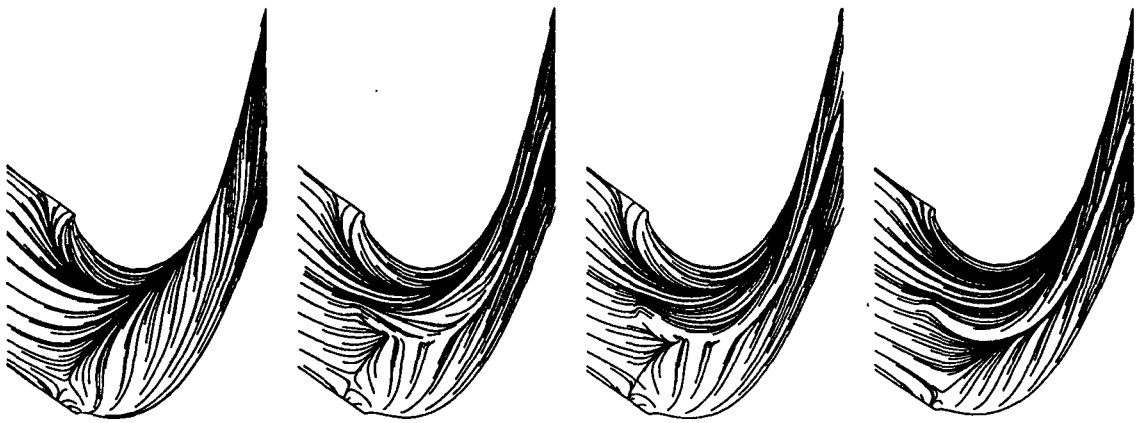

(c) Limiting streamlines on the endwall.

Fig. 7 Visualizations of the secondary flow structures in turbine cascades with and without endwall fences.

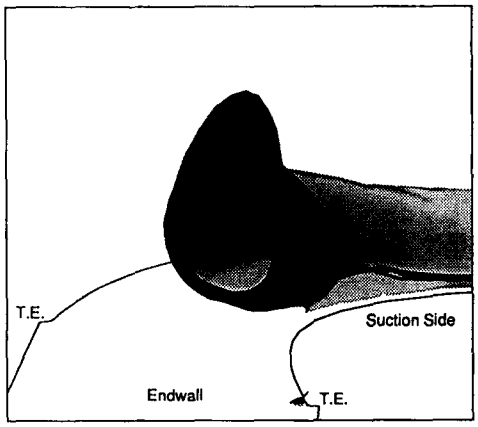

(a) No fence.

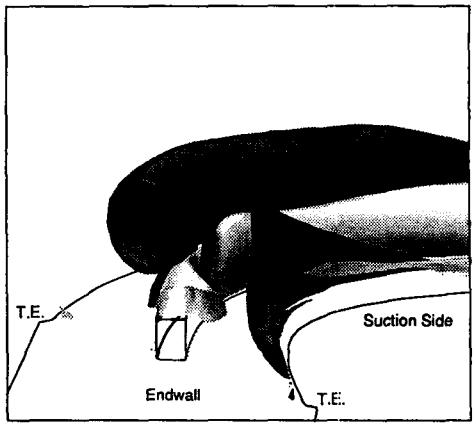

(b) $h_f=\frac{1}{3}\delta$ fence.

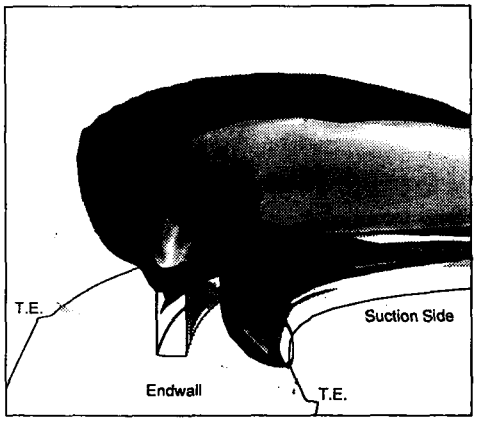

(c) $h_f=\frac{2}{3}\delta$ fence.

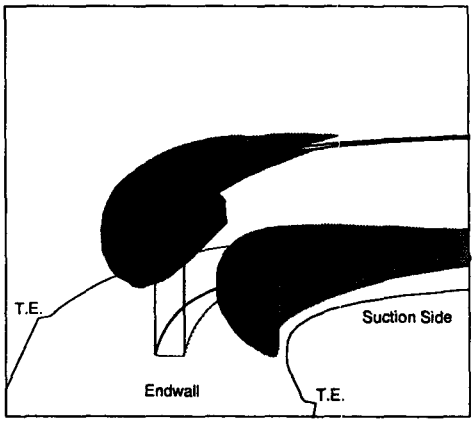

(d) $h_f=\frac{3}{3}\delta$ fence.

Fig. 8 Iso-surfaces of the non-dimensional streamwise vorticity ($C\omega_s/U = -15, 15$) along the cascade flow passage, illustrating the formation of a counter-rotating streamwise vortex.